AIAA JOURNAL
Vol. 42, No. 9, September 2004

Testing of Stiffened Composite Cylindrical Shells in the Postbuckling Range Until Failure

Chiara Bisagni* and Potito Cordisco†
Politecnico di Milano, 20156 Milan, Italy

The results of an experimental investigation of two stringer-stiffened shells and of two ring- and stringer-stiffened cylindrical shells made of carbon fabric reinforced plastic are presented. The specimens are tested until collapse by means of custom-made biaxial testing equipment that allows axial and torsion loading, applied separately and in combination, using a position control mode. This apparatus includes a laser scanning system for the measurement in situ of the geometric imperfections, as well as of the progressive change in deformations. The experimental data acquired during the first nondestructive buckling tests and during the destructive failure tests clearly demonstrate the strength capacity of these structures to work in the postbuckling field, allowing for the further weight savings likely to be requested in the near future for the construction of aerospace structures. Indeed, the results show that the shells are able to sustain load in the postbuckling field without any damage, whereas the collapse, both under axial compression and under torsion, due to the failure of the stringers is sudden and destructive. The measured data can be used for the development and validation of analytical and numerical high-fidelity methods and, together to these validated analysis tools, to provide design criteria that are less conservative than those presented.

Introduction

RECENT advances at NASA in the development of aircraft structures and launch vehicles have indicated that existing monographs on cylindrical shell stability need to be updated and expanded.[1,2] For example, the original NASA monographs[3] that report recommendations for the design of buckling-resistant cylindrical structures provide reliable, but often overly conservative means of designing shells by the use of simple, linear analytical models and an empirical correction factor, the "knock-down factor." Likewise, these reports contain practically no design information for lightweight high-performance composite shells.

The interest in updating the monographs is mainly driven by significant advances in computer technology and computational analysis tools, as well as in experimental methods and techniques.

The improved computational analysis tools have made it possible to introduce more sophisticated analytical and numerical models for the nonlinear shell response, allowing investigation of complex geometries, loading conditions, boundary conditions, as well as the introduction of initial geometric imperfections. The nonlinear buckling behavior of several structures has been studied numerically in recent years, such as stiffened shells in offshore applications[4] and a liquid-oxygen tank to serve as a new space shuttle superlightweight external fuel tank.[5]

Numerical simulation has proven capable of performing structural optimization of composite panels under buckling, postbuckling, and strength constraints[6–9] and can be used to establish shell buckling behavior trends and perform sensitivity studies on a wide range of parameters for the definition of design recommendations.[10–13]

The analytical and numerical models need to be validated with test results before they can be used with full confidence. At the same time, the advancements in experimental methods and techniques provide more carefully controlled experiments and high-fidelity test results.[14] A selective testing approach, in conjunction with numerical simulations, is particularly important when the costs of conducting experiments and the costs of test specimens such as those made of fiber-reinforced composite materials are considered. Consequently, selective experiments can be identified and accurately conducted to establish credible design recommendations.

For example, technology is now available to measure accurately the initial geometric imperfections of composite shell test specimens[15,16] that can be used as inputs to the international imperfection data bank for comparative studies on the effect of the manufacturing process on the magnitude and spatial distribution of the geometric imperfections.[17,18] Furthermore, they can be introduced in the numerical models to understand the effect of the initial geometric imperfection shape and amplitude on the composite shells.[11,19]

New combined load test capabilities have been developed at Politecnico di Milano, and selective fiber-reinforced composite cylindrical shells have been tested to investigate the effect of axial compression and torsion applied individually and in combination.[14,20–23]

Experimental data available for composite cylindrical shells are still scarce, especially in the postbuckling range all of the way to failure. On the other hand, further weight savings, likely to be needed in the near future for aerospace structures, can be reached with composite stiffened structures by allowing them to operate in the postbuckling range, as is the case for metallic structures. For this reason, the postbuckling response must be clearly identified and understood, as well as the collapse load and the collapse mode, through selective experiments.

The present paper describes the results of an experimental investigation on two stringer-stiffened cylindrical shells and on two composite ring- and stringer-stiffened cylindrical shells made of carbon fabric reinforced plastic (CFRP). After measurements of the geometric imperfections, tests are performed under axial compression and torsion, by the use of a position control mode, applied individually and in combination. Then, the two stringer-stiffened cylindrical shells were tested until collapse under axial compression and the two ring- and stringer-stiffened cylindrical shells were tested until collapse under torsion. The experimental data acquired during the first nondestructive buckling tests and during the destructive collapse tests can help in the investigation of the load-carrying capacity of these structures, with regard to their ability to work in the postbuckling field without damage, and can be used, together to high-fidelity analysis methods, to develop design criteria less conservative than those presented.

Received 27 October 2003; revision received 17 March 2004; accepted for publication 30 March 2004.

*Assistant Professor, Dipartimento di Ingegneria Aerospaziale, Via La Masa 34; Chiara.Bisagni@polimi.it. Member AIAA.

†Research Assistant, Dipartimento di Ingegneria Aerospaziale, Via La Masa 34; Cordisco@aero.polimi.it.

Cylindrical Stiffened Shells

The four specimens were fabricated by Agusta helicopter company in Italy from a CFRP fabric tape material. The material was laid up on a mandrel and cured in an autoclave to form four shells of two different configurations.

Both of the configurations present the same geometrical dimensions: an internal radius of 350 mm and a length of 700 mm. The actual length of the specimens is limited to the central part of the cylinder height and is equal to 540 mm. This is due to the necessity of including two tabs at the top and at the bottom of the shells, to permit fixing into the test facility. The lamina material properties, reported in Table 1, are experimentally obtained by tests performed according to the Independent European Program Group guidelines.[24]

The two configurations were designed to be able to work in the postbuckling range. Consequently, the number of stiffeners and their layups were optimized to guarantee a local skin buckling after the critical buckling load and before the final collapse. In particular, the first configuration was designed to offer a ratio between the collapse load and the first buckling load under axial compression equal to about three. The second configuration was intentionally designed to work under torsion, offering a ratio between the collapse torque and the first buckling torque equal to about three. Consequently, two stringer-stiffened cylindrical shells were fabricated for the first configuration and two ring- and stringer-stiffened cylindrical shells for the second configuration. Indeed, the presence of a central reinforcing ring, cocured on the external surface at one-half of the height of the cylinder, has been demonstrated to be the best method to increase the postbuckling range under torsion without the influence of buckling torque.[25,26]

Table 1 CFRP lamina material properties

Property	Lamina
Young's modulus E_{11}, N/mm^2	57,765
Young's modulus E_{22}, N/mm^2	53,686
Shear modulus G_{12}, N/mm^2	3,065
Poisson's ratio ν_{12}	0.048
Density ρ, kg/mm^3	1,510
Ply thickness, mm	0.33

The first configuration (Fig. 1a) is characterized by eight stringers, L-shaped, equally oriented and equally spaced in the circumferential direction. The details of the skin and stiffener layups are shown in Fig. 1b. The blade of the stiffeners is 25 mm long, whereas the flange attached to the skin of the cylinder is 32 mm long. The stiffeners present a rounded corner, with an average radius of 7 mm, due to the manufacturing process. The skin of the cylinder is made of 2 plies, [±45 deg] oriented, whereas the stringers consist of 12 plies $[0\ \text{deg}/90\ \text{deg}]_{3s}$ oriented, where 0 deg is the axial direction of the shell. In correspondence with the stiffeners, on the outer side of the skin, three reinforcement layers [0 deg/45 deg/−45 deg] are added. The reinforcements are 40 mm and 700 mm long in the circumferential and in the axial direction, respectively. The stringers are bonded to the skin, and then nine rivets are added for each stringer for safety in case of debonding.

The second configuration (Fig. 1c) consists of ring- and stringer-stiffened cylindrical shells. The details of the skin and stiffener layups are shown in Fig. 1d. The stringers are equal in number and

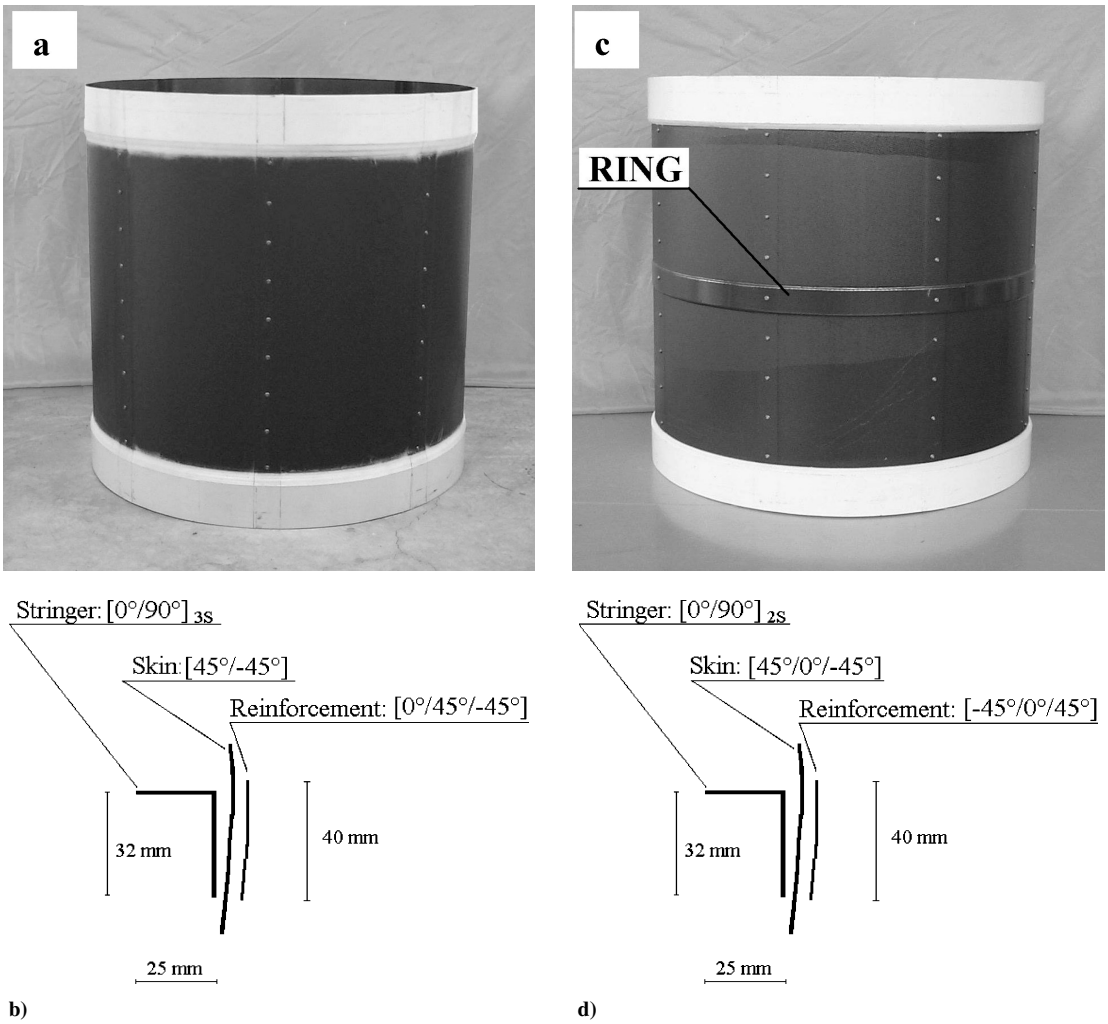

Fig. 1 Test specimens: a) stringer-stiffened shell, b) details of the skin and stiffener layups, c) ring- and stringer-stiffened shell, and d) details of the skin and stiffener layups.

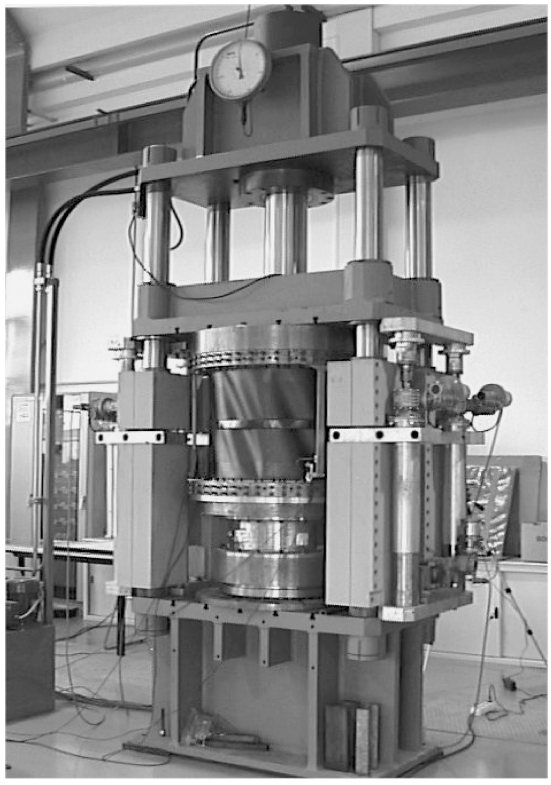

Fig. 2 Buckling test facility.

dimension to those of the first configuration, but consist of eight plies $[0\ \text{deg}/90\ \text{deg}]_{2s}$ oriented. The skin of the cylinder is made of three plies [45 deg/0 deg/−45 deg], whereas the reinforcements in correspondence with the eight stringers are obtained by the addition of three layers [−45 deg/0 deg/45 deg] on the outer side of the skin. Moreover, this configuration is characterized by a reinforcing ring in the central part of the cylinder. The ring is 40 mm high and consists of eight plies $[0\ \text{deg}/90\ \text{deg}]_{2s}$ oriented. Like the vertical stringers, the reinforcing ring is bonded to the outer side of the skin and then riveted in correspondence with the stiffeners.

Test Apparatus

The test facility, shown in Fig. 2, was used in buckling tests under axial compression, torsion, and combined axial compression and torsion, by the use of a position control mode. A detailed description of the test apparatus is presented in Refs. 21 and 23. For clarity, the main characteristics of the test facility and of the experimental process are summarized here.

During axial compression tests, the load is provided by a hydraulic ram, but the load level, which is transferred smoothly to the cylinder, is governed by the axial displacement of the upper loading platform. Indeed, this displacement is computer-controlled, moving four stepping motors connected to four ball screws placed at the four corners of the loading platform. During torsion tests, the rotation is given to the specimen bottom by a torsion lever. The lever motion is computer-controlled, producing the desired displacement of a screw by a stepping motor. The equipment allows the application of axial compression and torsion in any desired sequence.

During the tests, three linear variable differential transformers (LVDTs) give directly the axial displacement of the specimen, measuring the distance between the upper clamp and the lower clamp.

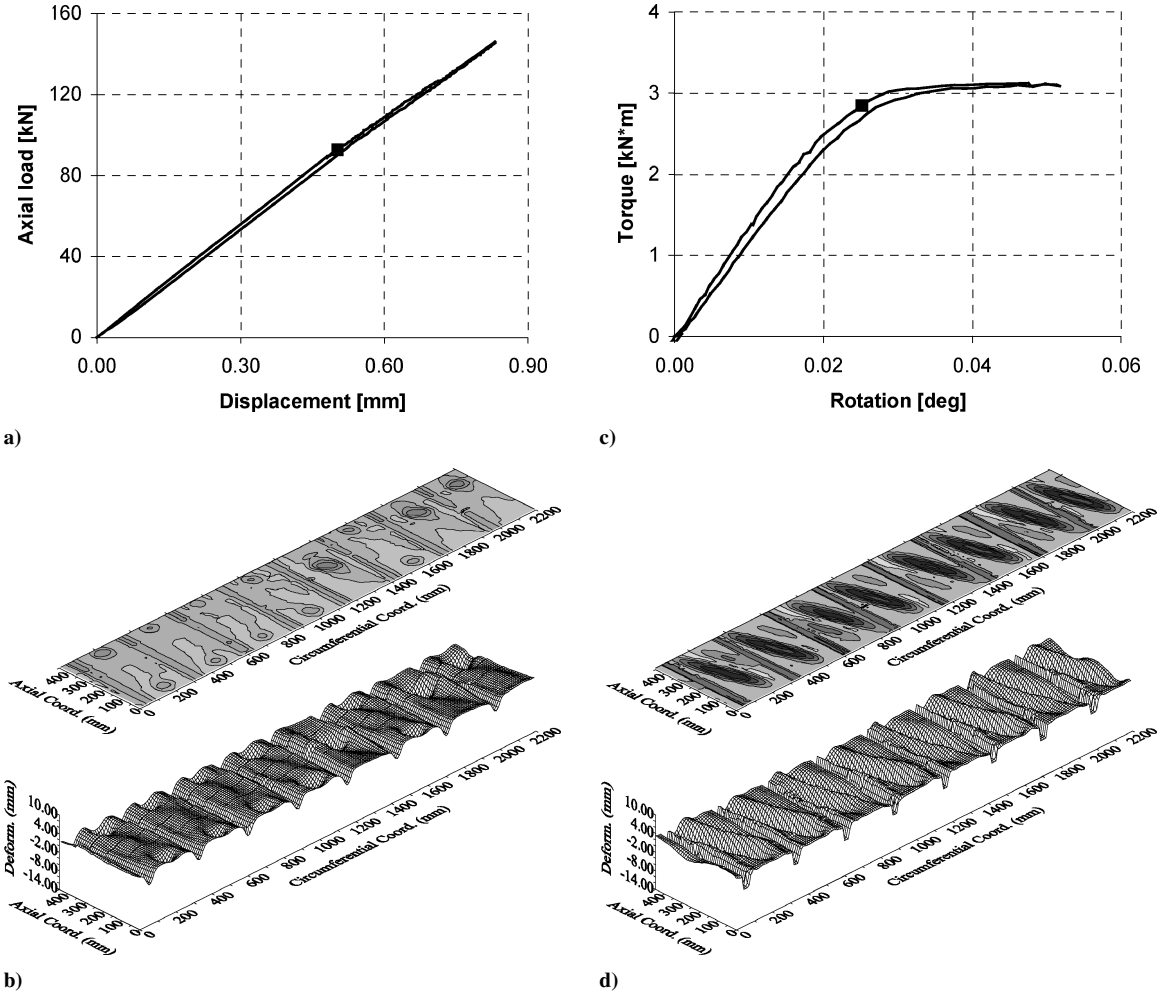

Fig. 3 Tests until local buckling of the first shell of the first configuration for the axial compression test: a) diagram of axial load vs displacement and b) postbuckling mode, and for the torsion test: c) diagram of torque vs rotation and d) postbuckling mode.

Three additional LVDTs measure the tangential displacement of the specimen bottom with respect to the top. A load cell, situated under the lower platform, is used to measure both the compression load and the torsion moment.

The inner surface of the specimens is scanned by means of an optical system consisting of five laser displacement sensors. They are placed inside the specimen at the distance of 40 mm, avoiding any contact with the specimen and, consequently, without influencing the buckling behavior, thus guaranteeing a measurement range of ± 15 mm with a resolution of 15 μm. Hence, it is possible to measure the inner surface in terms of geometrical imperfections (some tens of micrometers), prebuckling shape, and progressive change of postbuckling deformations (about 10–20 mm). Measurements of the inner surface are taken over a uniform grid with steps of 10 mm in the axial direction and 10 mm (approximately 0.03 deg of arc) in the circumferential direction. The time required to scan the whole inner surface is only 4 min.

Test Procedure

After that, each specimen is mounted in the test apparatus, the geometric imperfections are measured in situ, and they are then processed by custom-developed software that calculates the best-fit cylinder through the entire grid of measured points. This widely used data processing technique permits, on one hand, an easy introduction of the imperfections into the analytical and numerical models[11,19] and, on the other, allows the imperfections to be used as inputs to the international imperfection data bank for comparative studies on the effect of the manufacturing process on the magnitude and spatial distribution of the geometric imperfections.[2,17,18]

The first specimen of each configuration is first tested until the local buckling load is reached under pure axial compression and under pure torsion, respectively. Then combined tests under axial compression and torsion are carried out until the local buckling loads are reached. These tests are performed two to three times to verify the repeatability of the obtained results. Finally, the collapse test is executed. In contrast, on the second specimen of each configuration, only the collapse test is performed. This allows for evaluation of the effect of the repeated buckling on the postbuckling cycles by comparison of the results obtained for the two nominally identical specimens of a single configuration. The modality of the collapse tests changes according to the configuration: The shells of the first configuration are collapsed under axial compression, whereas collapse tests under torsion are carried out on the specimens of the second configuration.

During the torsion tests, to perform completely displacement-controlled tests, it was decided to constrain the axial displacement of the upper loading platform and to apply a controlled rotation to the lower one. Because the axial shortening of the cylinders is constrained, a considerable axial reaction force develops in the tests.

For combined tests, the specimen is twisted in the counterclockwise direction to a predetermined value of torque, and then axial compression is applied until local buckling is reached. In previous work on unstiffened CFRP cylindrical shells, it was noted that the sequence of application of axial compression and torsion in the combined tests influence neither the buckling load nor the buckling deformation.[23]

In all of the tests, axial displacement is applied in steps of about 0.005 mm, whereas angular rotation steps of about 0.0005 deg are imposed via software. After each step, the effective values of

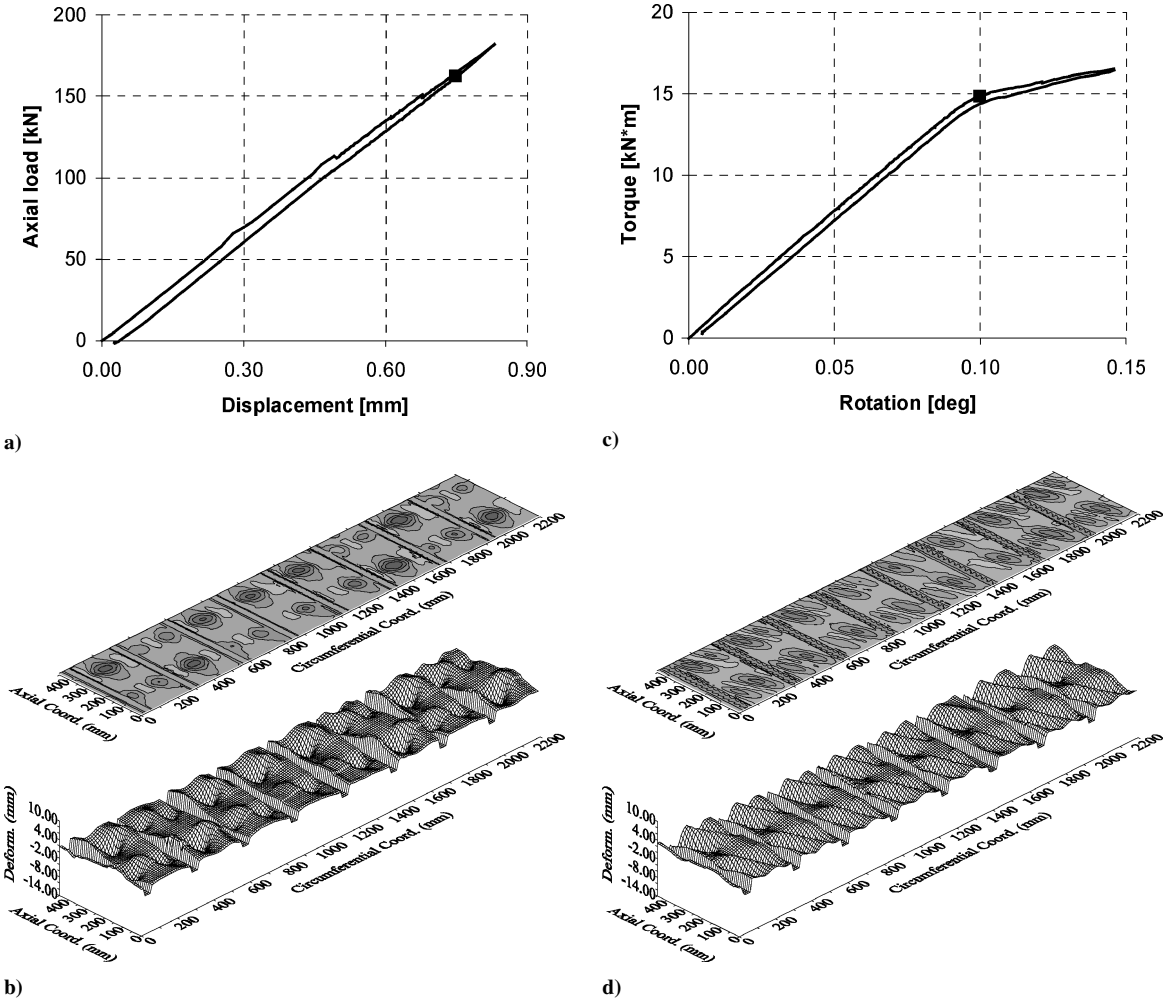

Fig. 4 Tests until local buckling of the first shell of the second configuration for the axial compression test: a) diagram of axial load vs displacement and b) postbuckling mode, and for the torsion test: c) diagram of torque vs rotation and d) postbuckling mode.

Table 2 Local buckling loads for axial compression and torsion tests: first specimen of the first configuration

Buckling	First test in axial compression	Second test in axial compression	Third test in axial compression	First test in torsion	Second test in torsion
First load	92.7 kN	92.5 kN	92.6 kN	3.0 kNm	2.8 kNm
First displacement	0.515 mm	0.503 mm	0.521 mm	0.027 deg	0.025 deg

Table 3 Local buckling loads for axial compression and torsion tests: first specimen of the second configuration

Buckling	First test in axial compression	Second test in axial compression	First test in torsion	Second test in torsion	Third test in torsion
First load	162.5 kN	172.5 kN	14.7 kN	14.8 kN	14.8 kN
First displacement	0.747 mm	0.741 mm	0.097 deg	0.099 deg	0.097 deg

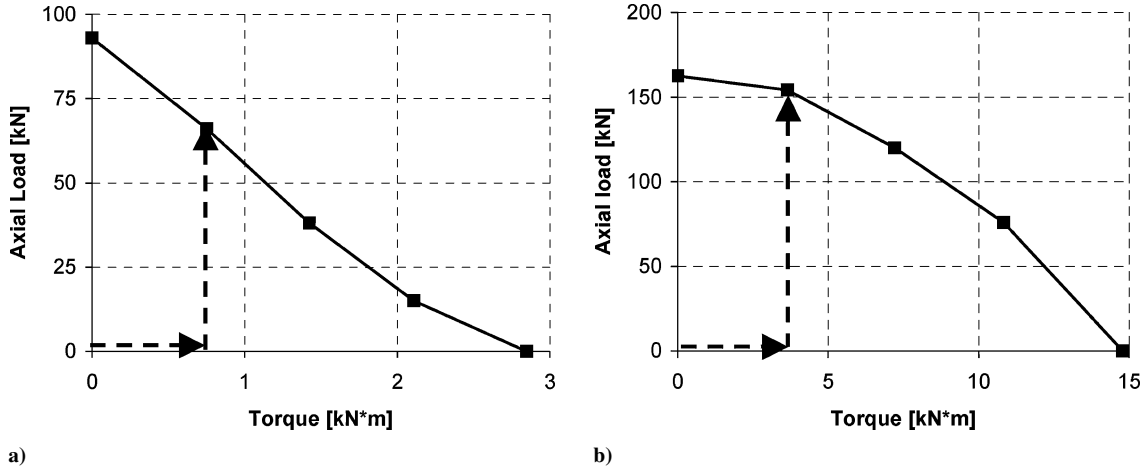

Fig. 5 Results of compression–torsion buckling tests: a) first and b) second configuration.

displacement, rotation, axial load, and torsion moment are measured by the six LVDT and the load cell. The curves of axial load vs displacement and of torque vs rotation are out lined in real time during the tests. In each test, the inner surface of the cylinder is measured several times, according to the duration of the test (typically, from 7 times for a pure compression test until the first local buckling to 30 times for a collapse test). This permits evaluation of the evolution of the surface from the undeformed prebuckling shape to the deformed postbuckling one. Moreover, collapse tests are digitally recorded by a double high-resolution camera system to detect the zones of the shell where the failure starts from, as well as its modality.

Tests Until First Local Buckling Under Axial Compression and Torsion Applied Separately

In the first round of tests, one specimen was tested three times under pure axial compression until local buckling. Table 2 presents the obtained first buckling loads and the corresponding axial displacements. The difference among the measured buckling loads is less then 1%.

Figure 3a depicts a typical axial load vs displacement curve and presents both the load and the unload phases. Note that stiffness did not change after local buckling. The reason is that the largest part of the load is supported by the stringers, which continue working even after the buckle of the skin. This is due to both the number of plies and their orientation. Indeed, whereas the skin is composed of only two [45 deg/−45 deg] plies, the stringers are made by the superimposition of 12 plies $[0\ \text{deg}/90\ \text{deg}]_{3S}$ oriented. Figure 3b shows, instead, a typical postbuckling shape. It is characterized by the presence of two small half-waves in five sectors and by a bigger single half-wave in the remaining three sectors. The maximum displacements normal to the surface recorded in the postbuckling field during these tests are equal to 6 mm inward and to 3.5 mm outward.

Then, two torsion tests were performed: The obtained buckling torque and the corresponding displacement are reported in Table 2.

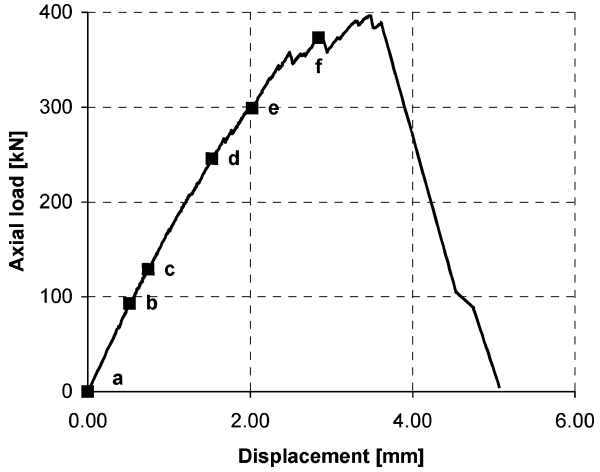

Fig. 6 Axial load vs displacement of the collapse test on the first shell of the first configuration.

Even these tests' results are repetitive, with a difference equal to 7% in the buckling torque.

Figure 3c shows a typical torque vs rotation curve. The kink corresponds to the local buckling torque. Under torsion, indeed, the role played by the axial stringers is negligible, and so the stiffness of the specimen sensibly decreases after the skin buckles. Even if the load and the unload parts of the curve do not perfectly superimpose, no residual deformations are recorded when torque is zero.

Figure 3d presents a typical postbuckling shape. In this case, the stable postbuckling mode, which is the same for the two tests, is characterized by the presence of a diagonal well-defined and perfectly regular wave in each sector. The displacements normal to the surface of the cylinder reach 9 mm inward and 5 mm outward.

The first specimen of the second configuration is, at first, tested twice until local buckling under pure axial compression. Table 3

lists the obtained results. By comparison of the values, it is possible to see a degree of repeatability: The difference is about 6% in load.

Figure 4a shows a typical axial load vs displacement curve. As in the first configuration, the slope of the curve did not change after the first local buckling load, and this is attributed to the presence of the axial stringers. Figure 4b instead presents a typical postbuckling deformed shape that is characterized by a single half-wave for each sector, between two consecutive axial stringers and the circumferential ring. The displacements normal to the surface reach 8 mm inward and 4 mm outward.

Then, three torsion tests are performed. Table 3 lists the results of the tests until local buckling, a result that is repetitive within a difference of 1% among the buckling torques.

The measured torque vs rotation curve is reported in Fig. 4c. As in the first local buckling, there is slope discontinuity. However, the specimen offers a residual stiffness due to the central reinforcing

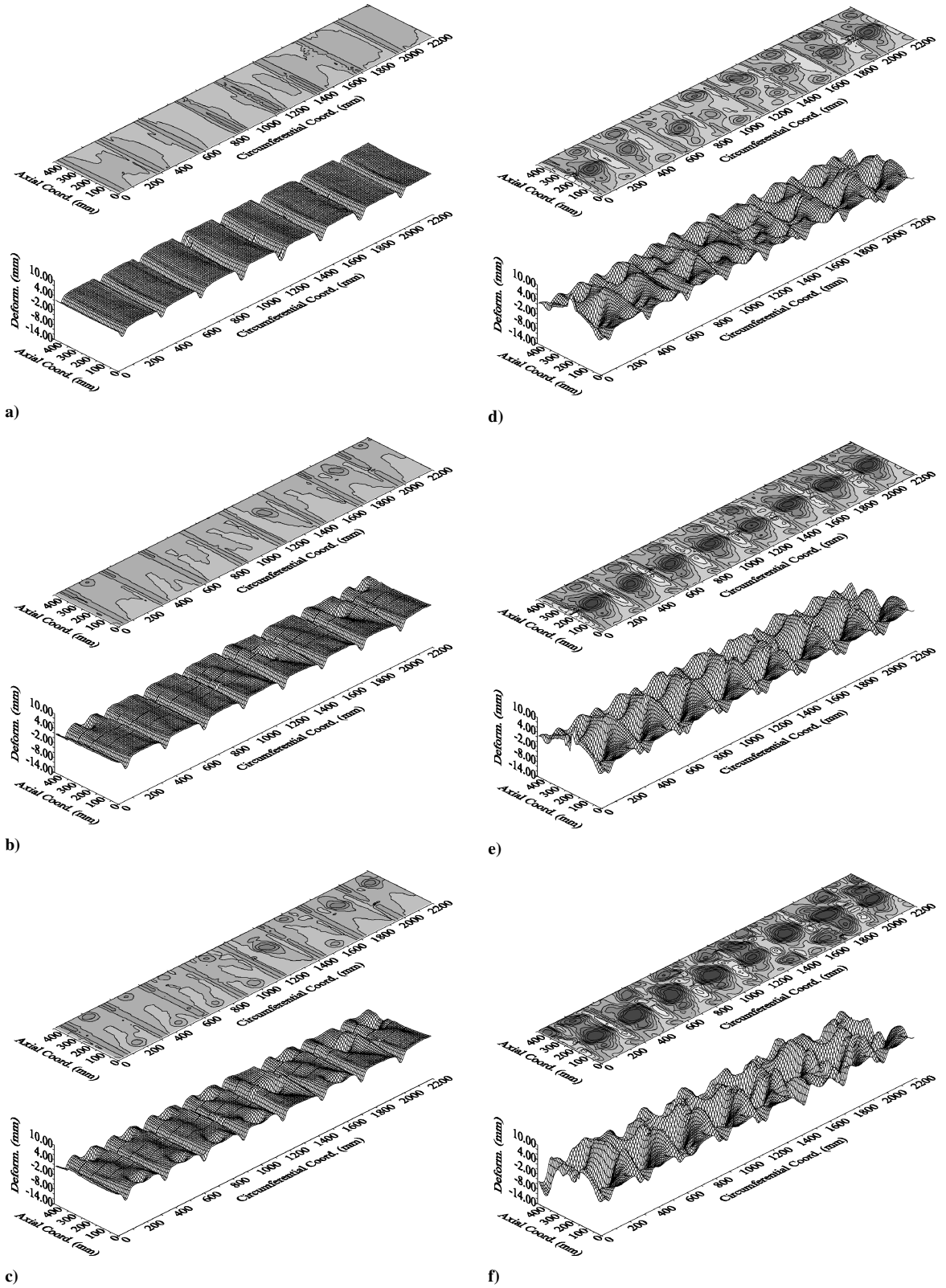

Fig. 7 Internal surface of the first shell of the first configuration during the collapse test: a) 0 kN, 0 mm; b) 93 kN, 0.515 mm; c) 128.9 kN, 0.746 mm; d) 245.4 kN, 1.530 mm; e) 298.6 kN, 2.025 mm; and f) 372.8 kN, 2.843 mm.

ring, and it is still able to sustain torsion load. Figure 4d shows the obtained internal surface map. The postbuckling mode is characterized by a diagonal wave in each sector.

Tests Until First Local Buckling Under Combined Axial Compression and Torsion

Three combined tests are carried out on the first cylinder of each configuration. The results are listed in Table 4. They are performed via twisting of the cylinder to one-, two-, and three-thirds of the buckling torque measured during the pure torsion test, respectively, and then under increasing axial load until the specimen locally buckles.

Figure 5 shows the obtained interaction curves for the two configurations.

The interaction curve of the first configuration presents a quasi-constant slope. The transition of the postbuckling deformed shape from the one obtained in the pure compression test to the one obtained in the pure torsion test is gradual. The interaction curve of the second configuration starts with a low gradient for a low value of the applied torque and, at about one-half of the buckling torque recorded in the pure torsion test, it suddenly increases the slope and maintains it almost constantly as the applied torque increases. It is possible to associate the change in the slope of the curve to the change in the deformed shape; parallel to the increase in the gradient, the postbuckling mode of the cylinder changes from a shape more similar to that of the pure compression test to a shape more similar to that of the pure torsion test. This is in perfect agreement with the results presented in a previous work[23] for unstiffened cylindrical specimens, likewise made of CFRP.

Table 4 Buckling loads for combined compression and torsion tests

First configuration		Second configuration	
P_{ax}, kN	M_t, kNm	P_{ax}, kN	M_t, kNm
92.7	0	172.5	0
66.0	0.7	154.0	3.6
38.1	1.4	119.9	7.2
15.1	2.1	75.8	10.8
0	2.8	0	14.8

Collapse Tests Under Axial Compression on the Two Shells of the First Configuration

The first and second specimen of the first configuration are then tested until collapse under axial compression, and the obtained results are presented in Table 5.

The axial compression load vs displacement for the first cylinder is presented in Fig. 6, where some points are highlighted in correspondence with the measured surfaces reported in Fig. 7. The curve presents a constant slope in its first part, even after the first local buckling occurs at 93 kN (point b in Figs. 6 and 7b). At about 128 kN (point c in Figs. 6, 7c, and 8a) the deformation has already spread all over the skin and is characterized by a double series of

Table 5 Collapse tests under axial compression of the two specimens of the first configuration

Specimen	1	2
First buckling load, kN	93.0	103.3
First buckling displacement, mm	0.515	0.539
Collapse load, kN	388.2	380.3
Collapse displacement, mm	3.611	3.210

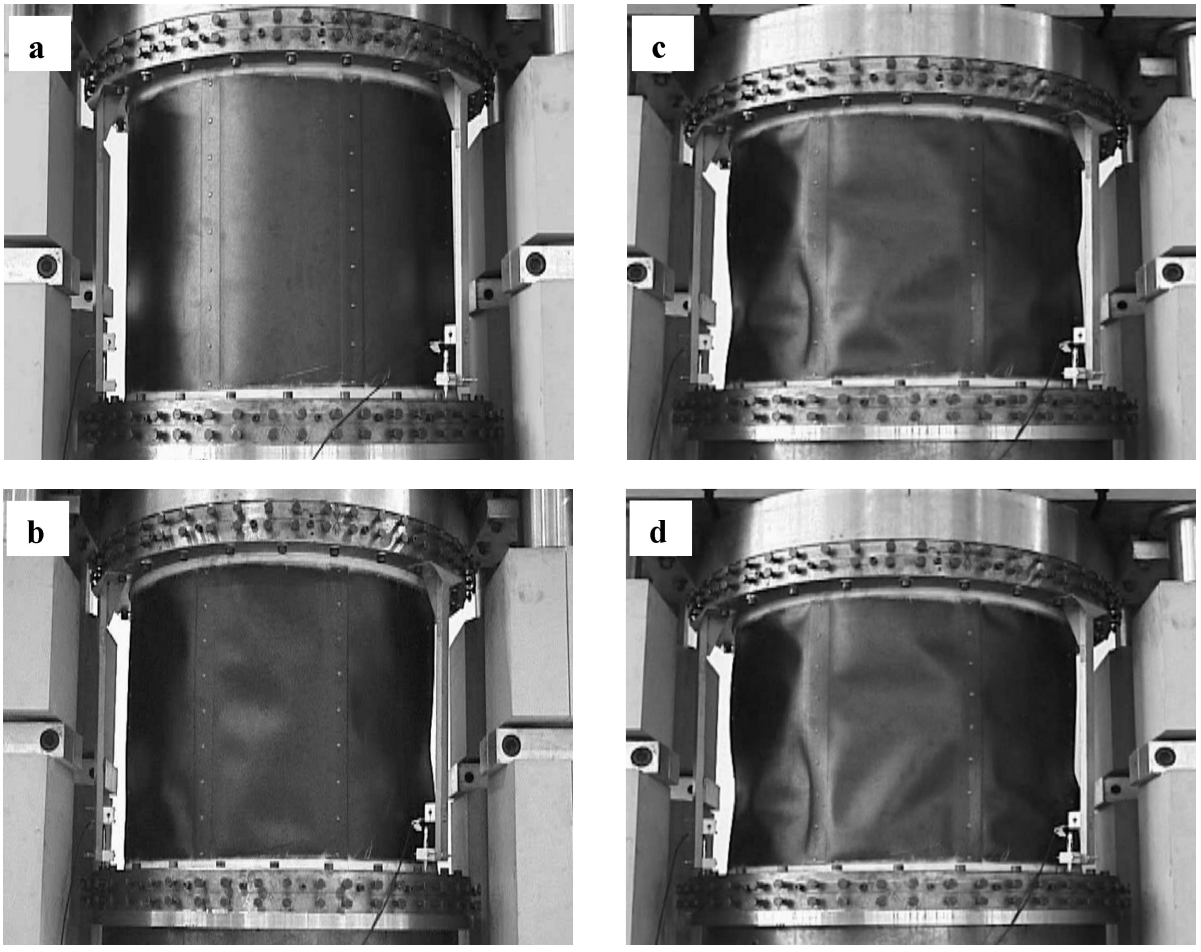

Fig. 8 Photographs of the postbuckling mode during the collapse test under axial compression.

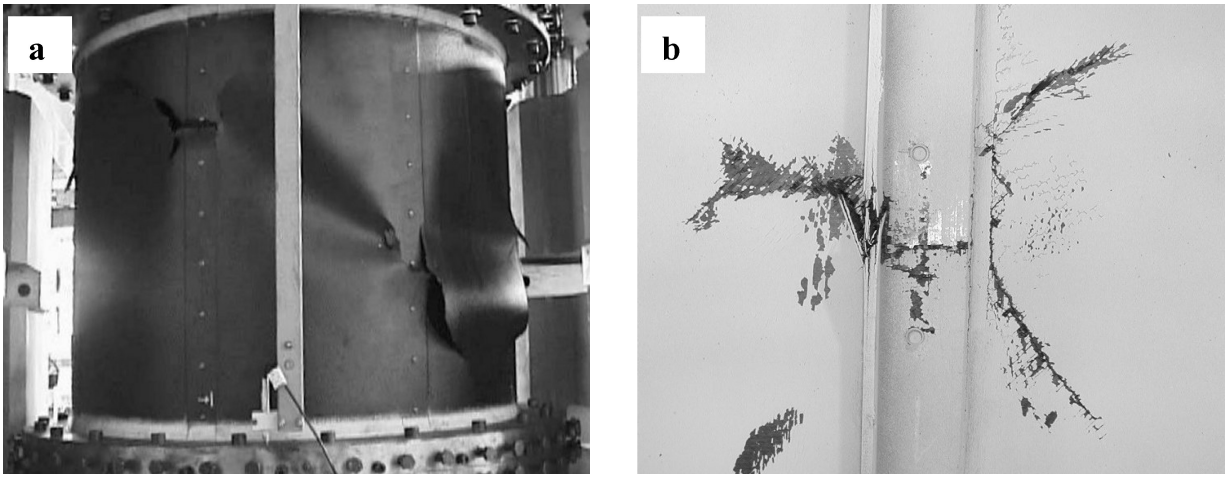

Fig. 9 Photographs of the collapse mode under axial compression.

half-waves in five sectors and by a single, bigger half-wave in the remaining three sectors. A third series of half-waves appears at about 250 kN (point d in Figs. 6 and 7d), whereas at 290 kN the waves in a single sector evolve, in the center of the specimen, in a single large half-wave (Figs. 7e and 8b). At this load, the mean displacements normal to the surface reaches 12 mm both inward and outward.

In the postbuckling range, the change in load distribution and the large increase in load carrying shared by the stiffeners causes the buckling of the stiffeners (Fig. 8c). At about 357 kN, a progressive reduction in the stiffness associated with drops in load starts, probably due to the buckling of the stiffeners, causing a reduction in the slope of the curve. With a further increase in axial displacement, the displacements normal to the surface also increase, reaching 14 mm inward and 12 mm outward (Figs. 7f and 8d).

Neither failure mechanisms nor hazards are visible in the postbuckling range. Only mild noises, possibly connected with limited delamination, are heard just before the collapse, which occurs at 388 kN both suddenly and intensively audibly. Collapse is caused by the simultaneous breakage of all of the stringers. The failure mechanisms start from the stringers in the central area of the cylinder height, far from the clamping rings, then causing extensive fracture in the skin and in the stringers (Fig. 9a). The phenomenon is similar to the crippling of metallic structures[27] because there is a local collapse in the stringers because the limit values are reached. This causes the energy release in the failure area and, consequently, extensive fracture both in the stringers and in the adjacent skin. No damage or failure occur at the stiffener-skin interface. The rivets do not break and no fracture starts from the rivets holes.

After the collapse, the specimen is not able to sustain the load any more and the load suddenly drops to about zero. The ratio between the collapse load and the first buckling load results equal to 4.2, showing a long postbuckling phase.

A photograph of stringer damage from inside the cylindrical shell after the specimen is taken out of the test facility is shown in Fig. 9b.

The second specimen of the first configuration is tested directly until collapse under compression. Figure 10 compares the axial compression vs displacement curve obtained for this shell to that one of the preceding shell. It is possible to see how the behavior in the prebuckling range and in the first part of the postbuckling field is practically the same, even if the second shell is slightly more rigid. (The stiffness difference is about 4.3%.) With regard to the evolution of the internal surface of the shell, it is the same as that of the first specimen and is omitted for this reason.

Whereas the difference in the collapse loads is about 2% (Table 5), the difference in the collapse displacements is about 11%. In this case, the ratio between the collapse and the first buckling load is equal to 3.7. Moreover, even if the collapse modality is the same as that of the preceding specimen, because it starts from the failure of the stringers, for this shell only five stringers break. By examination of the curve, indeed, it is possible to see that the load does not go to zero after collapse.

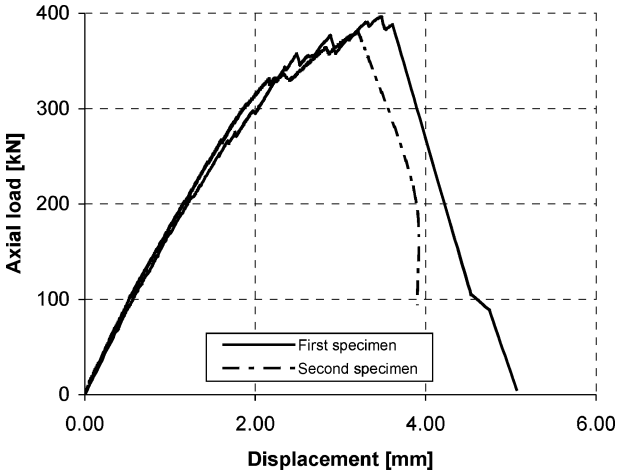

Fig. 10 Axial load vs displacement of the collapse tests on the shells of the first configuration.

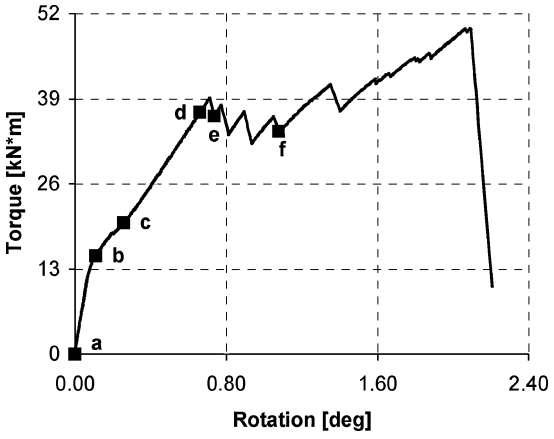

Fig. 11 Torque vs rotation curve of the collapse test on the second shell of the second configuration.

Collapse Tests Under Torsion on the Two Shells of the Second Configuration

A collapse test under torsion loading is performed on the first cylinder and on the second cylinder of the second configuration.

The significant data acquired during the tests are reported in Table 6, whereas the measured torque vs the rotation angle for the second cylinder is presented in Fig. 11, in which some points are highlighted in correspondence with the measured surfaces reported in Fig. 12.

Initially the slope is constant, followed by a kink corresponding to the first local buckling torque at 15 kNm. The buckling of the

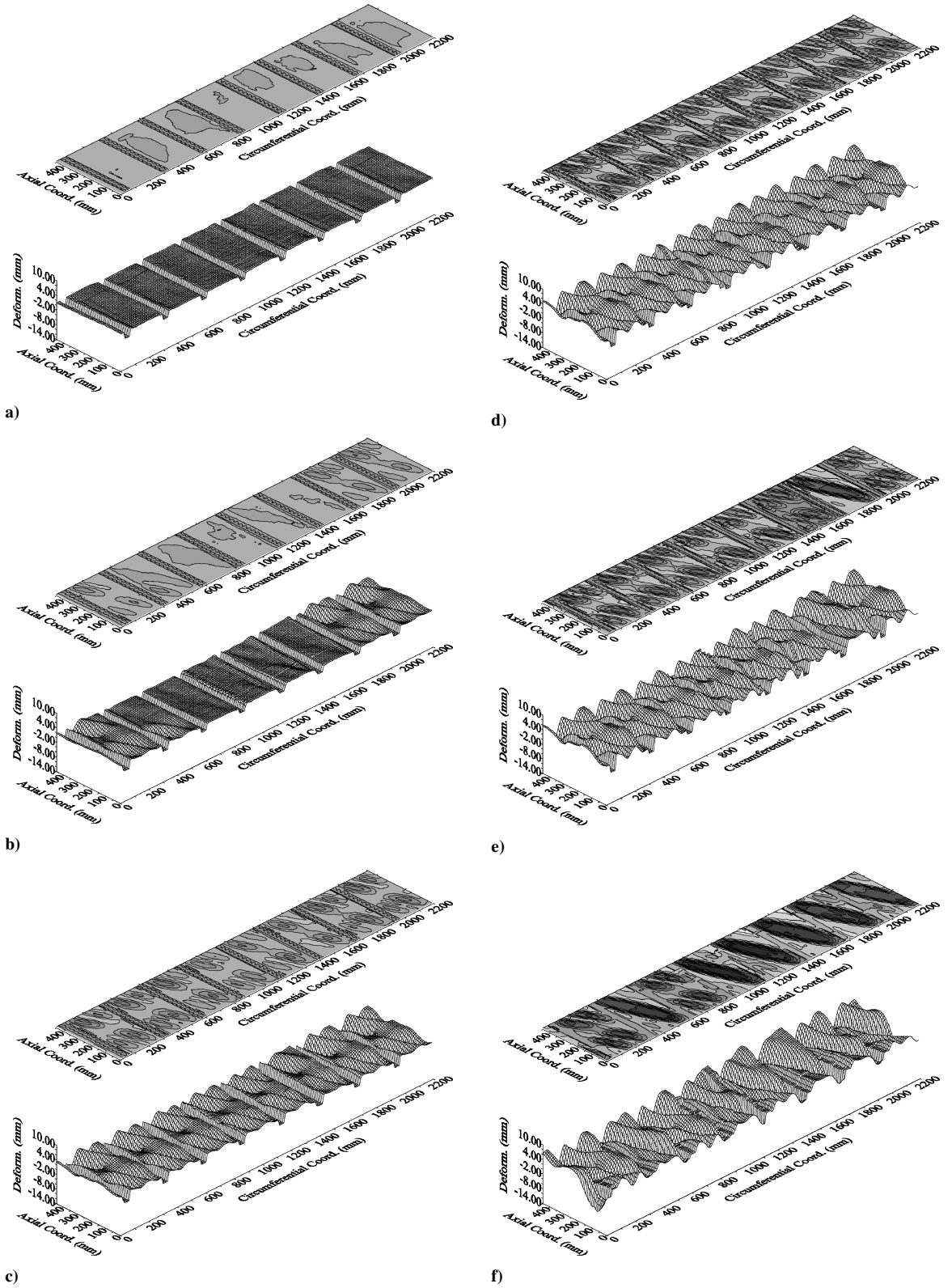

Fig. 12 Internal surface of the second shell of the second configuration during the collapse test: a) 0 kNm, 0 deg; b) 15 kNm, 0.109 deg; c) 30 kNm, 0.499 deg; d) 36.9 kNm, 0.660 deg; e) 36.3 kNm, 0.736 deg; and f) 34.0 kNm, 1.077 deg.

skin occurs, at first in four sectors (Fig. 12b) and then, as the torque increases, it evolves gradually to all of the other sectors. At 19 kNm, all of the skin is completely buckled (Figs. 12c and 13a). The cylinder presents two diagonal half-waves in each sector delimited by two stringers in the circumferential direction and by the external reinforcing ring in the axial direction. These waves are perfectly defined and have a regular shape. The normal displacements are of 5.5 mm inward and 3.5 mm outward.

The shell shows a postbuckling residual torsional stiffness equal to about 22% of the prebuckling shell because it is equal to 40 kNm/deg against a prebuckling value of 180 kNm/deg. The central reinforcing ring helps the specimen to carry torque even in the postbuckling phase.

By an increase in the torque, the out of the plane deformations increase, reaching 8 mm inward and 5 mm outward, but they do not change their shape (Figs. 12d and 13b) until, at about 39 kNm,

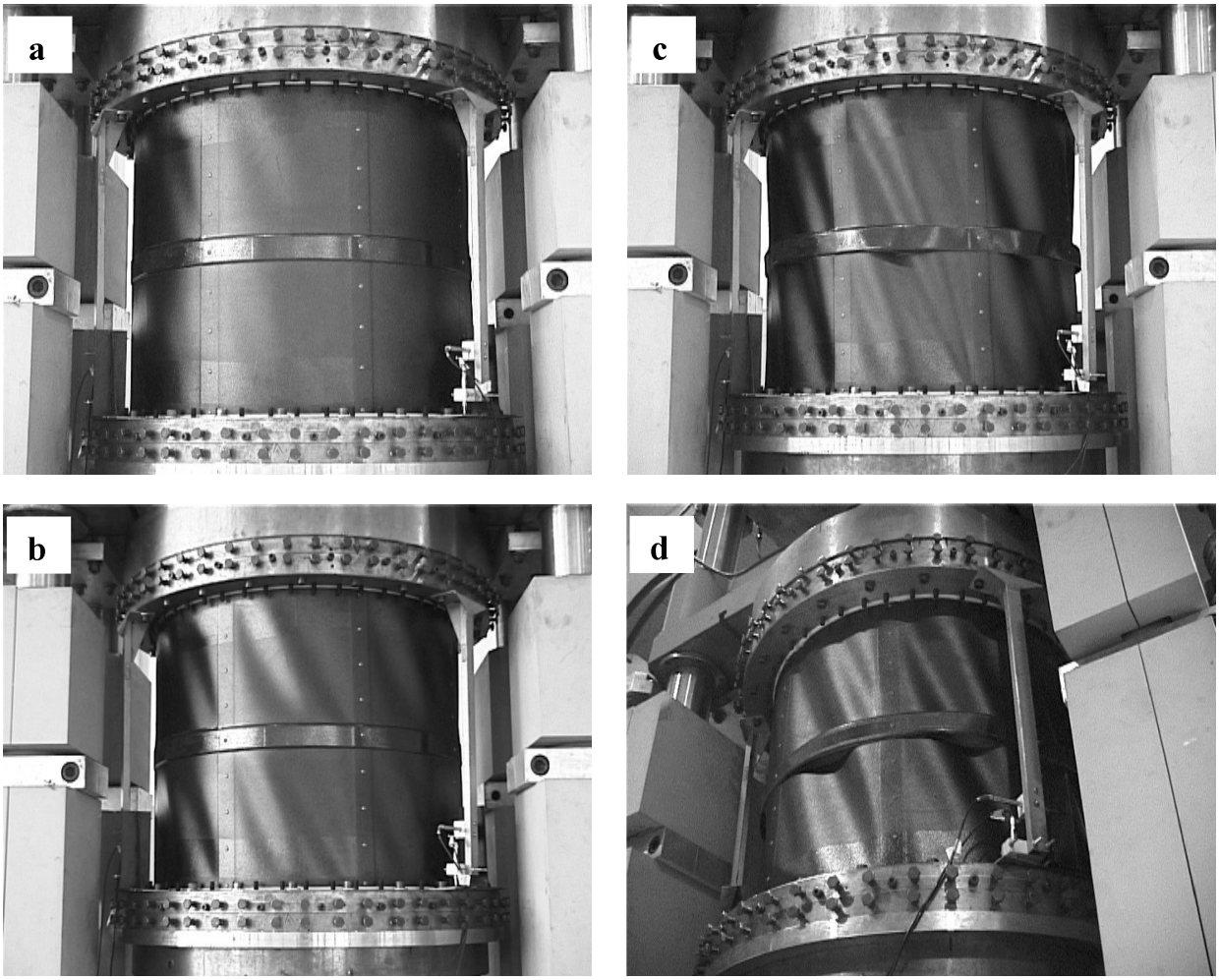

Fig. 13 Photographs of the postbuckling mode during the collapse test under torsion.

Table 6 Collapse tests under torsion of the two specimens of the second configuration

Specimen	1	2
First buckling torque, kNm	15.2	15.0
First buckling rotation, deg	0.100	0.109
First skin-ring separation torque, kNm	36.1	39.1
Rotation at first skin-ring separation torque, deg	0.640	0.711
Collapse torque, kNm	45.1	49.6
Collapse rotation, deg	1.616	2.093

with a rotation angle equal to about 0.7 deg, the central reinforcing ring debonds from the skin in one of the cylinder sectors (Fig. 12e). This is the direct consequence of the way the skin works under torsion. Indeed, the postbuckling pattern of a cylinder without a central reinforcing ring is characterized by ideal diagonal lines from the lower-right to the upper-left corners of each sector. In this way, traction stresses are concentrated along the bay diagonally, and the fibers of these skin areas are free to shorten significantly and to move internally with respect to the initial shell radius. This way of working is prevented here by the central reinforcing ring that, remaining of the same radius, constrains the panel skin to arrange along two different diagonal waves in each of the half-cylinder heights. Thus, by an increase in the torque, meaningful interlaminar stresses appear between the panel skin and the reinforcing ring and produce their separation. Once the central ring is debonded, the skin pattern suddenly changes.

As the torque increases again, the ring debonds in other sectors (Fig. 12f), and the radial displacements reach 14 mm inward and 10 mm outward. At a rotation of about 1.7 deg the circumferential ring is completely debonded from the skin and is connected to the skin only by the eight rivets that fix it to the stiffeners, as shown in the photographs in Figs. 13c and 13d. Unfortunately, at this rotation the laser scanning system was unable to measure the inner surface any longer because the stringers were already significantly buckled and touched the laser sensors.

The structural collapse occurs, intensively audibly and clearly visible, at a torque of 49.6 kNm and at an imposed rotation of 2 deg. The ratio between the collapsed torque and the first buckling torque equals 3.3. The collapse is due to the simultaneous breakage of four stiffeners. Even in this case, as was the case for the cylinders of the first configuration, the failure starts from the stringers and then suddenly evolves to the skin, as shown in Fig. 14a. In this case, due to the torque applied, the failure of the stringers starts near the clamping rings. As for the cylinders of the first configuration, the collapse is largely due to the compression of the stringers caused from the diagonal tensional field. A photograph of a stringer failure from inside the cylindrical shell after it is taken out of the test facility is shown in Fig. 14b.

Figure 15 presents the superimposition of the torque vs rotation curves obtained for the two cylinders of this configuration. The recorded values are reported in Table 6. The behavior of the two specimens is very close both in the prebuckling and in the postbuckling range up to the separation between the cylinder skin and the central ring. Also, the evolution of the internal surface of the first shell is the same as that of the second one, and, for this reason, it is omitted. A noticeable difference is, instead, shown in the collapse torque and in the corresponding rotation. The differences in the values are quite large: 10% for torque and 23% for rotation. The ratio between the collapse torque and the first buckling torque results equal three. It is difficult to see if the higher values of collapse

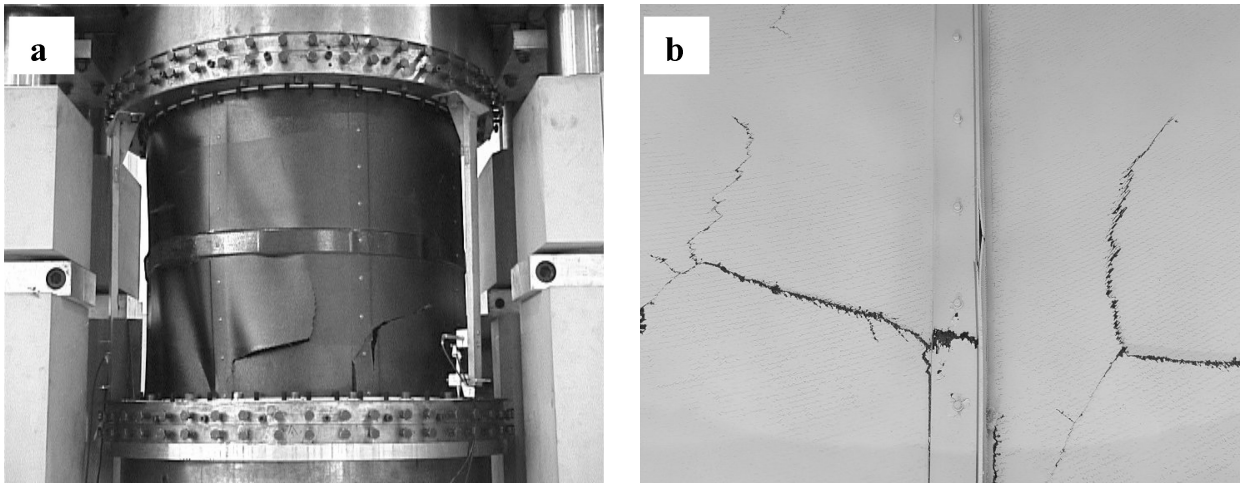

Fig. 14 Photographs of the collapse mode under torsion.

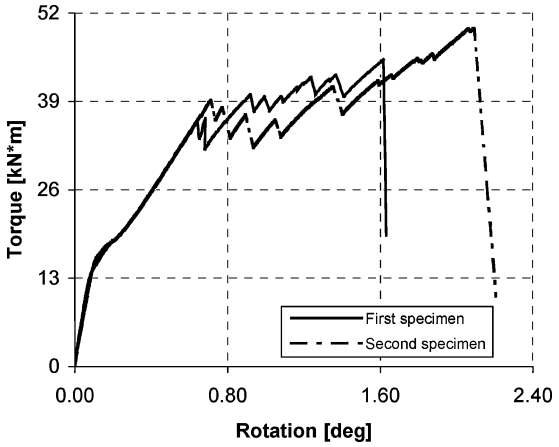

Fig. 15 Torque vs rotation curve of the collapse tests on the shells of the second configuration.

torque and rotation are because the shell was not earlier tested under repeated local buckling because the number of tested shells are few, and the behavior was the opposite for the first configuration.

Conclusions

The results of an experimental investigation on buckling and postbuckling behavior of four stiffened CFRP cylindrical shells were presented and discussed. After the measurements of the geometric imperfections, tests were performed under axial compression and torsion, by the use of a position control mode, applied individually and in combination. Then, two stringer-stiffened cylindrical shells were tested until collapse under axial compression, and the two ring- and stringer-stiffened cylindrical shells were tested until collapse under torsion. During the tests, the axial load, the torque, as well as the displacement and the rotation were measured with a load cell and six LVDTs, respectively. In addition, a laser scanning system measured the progressive change in deformations of the shells in the postbuckling field.

The data acquired during the first nondestructive tests and during the destructive collapse tests demonstrate that the shells are able to sustain load in the postbuckling field without any damage. Indeed, neither failure mechanisms nor any other hazards are visible in the postbuckling range. On the other hand, the collapse, due to the failure of the stringers both under axial compression and under torsion, is sudden and destructive. It causes extensive fracture in the skin and in the stringers, so that, after the collapse, the load suddenly drops to about zero.

The experimental data show clearly the strength capacity of these structures to work in the postbuckling range, allowing for the further weight savings likely to be required in the near future for the construction of aerospace structures. The ratio between the collapse load and the first buckling load was shown to be higher than 3.

The measured data can be also used for the development and validation of analytical and numerical high-fidelity methods and, together to these validated analysis tools, to provide design criteria that are less conservative than existing ones.

Acknowledgments

This work is supported by the European Commission, Competitive and Sustainable Growth Programme, Contract G4RD-CT-1999-00103, project POSICOSS. The authors are grateful to Vittorio Giavotto for sharing his expertise and for helping with many valuable suggestions. The information in this paper is provided as is and no warranty is given that the information is fit for any particular purpose. The reader thereof uses the information at its sole risk and liability.

References

[1]Nemeth, M. P., and Starnes, J. H., Jr., "The NASA Monographs on Shell Stability Design Recommendations," NASA TP-1998-206290, 1998.

[2]Arbocz, J., and Starnes, J. H., Jr., "Future Directions and Challenges in Shell Stability Analysis," *Thin-Walled Structures*, Vol. 40, 2002, pp. 729–754.

[3]"Buckling of Thin-Walled Circular Cylinders," NASA SP-8007, 1968.

[4]Das, P. K., Thavalingam, A., and Bai, Y., "Buckling and Ultimate Strength Criteria of Stiffened Shells Under Combined Loading for Reliability Analysis," *Thin-Walled Structures*, Vol. 41, 2003, pp. 69–88.

[5]Nemeth, M. P., Young, R. D., Collins, T. J., and Starnes, J. H., Jr., "Effects of Initial Imperfections on the Non-Linear Response of the Space Shuttle Superlightweight Liquid–Oxygen Tank," *International Journal of Non-Linear Mechanics*, Vol. 37, 2002, pp. 723–744.

[6]Nagendra, S., Jestin, D., Gürdal, Z., Haftka, R. T., and Watson, L. T., "Improved Genetic Algorithm for the Design of Stiffened Composite Panels," *Computers and Structures*, Vol. 58, No. 3, 1996, pp. 543–555.

[7]Wiggenraad, J. F. M., Arendsen, P., and da Silva Pereira, J. M., "Design Optimization of Stiffened Composite Panels with Buckling and Damage Tolerance Constraints," AIAA Paper 98-1750, 1998.

[8]Bisagni, C., and Lanzi, L., "Post-Buckling Optimisation of Composite Stiffened Panels Using Neural Networks," *Composite Structures*, Vol. 58, No. 2, 2002, pp. 237–247.

[9]Rikards, R., and Auzins, J., "Response Surface Method in Design Optimization of Carbon/Epoxy Stiffened Shells," AIAA Paper 2002-5654, 2002.

[10]Simitses, G. J., "Buckling and Postbuckling of Imperfect Cylindrical Shells: A Review," *Applied Mechanics Reviews*, Vol. 39, No. 10, 1986, pp. 1517–1524.

[11]Bisagni, C., "Numerical Analysis and Experimental Correlation of Composite Shell Buckling and Post-Buckling," *Composites Part B: Engineering*, Vol. 31, No. 8, 2000, pp. 655–667.

[12]Wullschleger, L., and Meyer-Piening, H.-R., "Buckling of Geometrically Imperfect Cylindrical Shells—Definition of a Buckling Load," *International Journal of Non-Linear Mechanics*, Vol. 37, 2002, pp. 645–657.

[13]Yap, J. W. H., Scott, M. L., Thomson, R. S., and Hachenberg, D., "The Analysis of Skin-to-Stiffener Debonding in Composite Aerospace Structures," *Composite Structures*, Vol. 57, 2002, pp. 425–435.

[14]Singer, J., Arbocz, J., and Weller, T., *Buckling Experiments—Experimental Methods in Buckling of Thin-Walled Structures*, Vol. 2., Wiley, New York, 2002.

[15]Chryssanthopoulos, M. K., Giavotto, V., and Poggi, C., "Characterization of Manufacturing Effects for Buckling-Sensitive Composite Cylinders," *Composites Manufacturing*, Vol. 6, No. 2, 1995, pp. 93–101.

[16]Chryssanthopoulos, M. K., Elghazouli, A. Y., and Esong, I. E., "Compression Tests on Anti-Symmetric Two-Ply GFRP Cylinders," *Composites Part B: Engineering*, Vol. 30, 1999, pp. 335–350.

[17]Arbocz, J., and Hol, J. M. A. M., "Collapse of Axially Compressed Cylindrical Shells with Random Imperfections," *Thin-Walled Structures*, Vol. 23, 1995, pp. 131–158.

[18]Singer, J., and Abramovich, H., "The Development of Shell Imperfection Measurement Techniques," *Thin-Walled Structures*, Vol. 23, 1995, pp. 379–398.

[19]Hilburger, M. W., and Starnes, J. H., Jr., "Effects of Imperfections on the Buckling Response of Compression-Loaded Composite Shells," *International Journal of Non-Linear Mechanics*, Vol. 37, 2002, pp. 623–643.

[20]Booton, M., and Tennyson, R. C., "Buckling of Imperfect Anisotropic Circular Cylinders Under Combined Loading," *AIAA Journal*, Vol. 17, No. 3, 1979, pp. 278–287.

[21]Bisagni, C., "Experimental Buckling of Thin Composite Cylinders in Compression," *AIAA Journal*, Vol. 47, No. 2, 1999, pp. 276–278.

[22]Meyer-Piening, H.-R., Farshad, M., Geier, B., and Zimmermann, R., "Buckling Loads of CFRP Composite Cylinders Under Combined Axial and Torsion Loading—Experiments and Computations," *Composite Structures*, Vol. 53, 2001, pp. 427–435.

[23]Bisagni, C., and Cordisco, P., "An Experimental Investigation into the Buckling and Post-Buckling of CFRP Shells Under Combined Axial and Torsion Loading," *Composite Structures*, Vol. 60, 2003, pp. 391–402.

[24]"Collection of Test Methods and Related Tools," Independent European Program Group, IEPG-CTP-TA 21 Guidelines, 1989.

[25]Lennon, R. F., and Das, P. K., "Torsional Buckling Behaviour of Stiffened Cylinders Under Combined Loading," *Thin-Walled Structures*, Vol. 38, 2000, pp. 229–245.

[26]Giavotto, V., Bisagni, C., and Lanzi, L., "Definition of Design Objectives and Constraints According to Results of WP1, Design and Analysis of the Verification Structures," Dipartimento di Ingegneria Aerospaziale, Technical Rept. WP2, Project POSICOSS GRD1-1999-10082, Politecnico di Milano, Milan, June 2002.

[27]Bruhn, E. F., *Analysis & Design of Flight Vehicle Structures*, Jacobs S. R. and Associates, Indianapolis, IN, 1973, pp. c7.1–c7.28.

K. Shivakumar
Associate Editor